

# Orthogonal stimulation of structural transformations in photo-responsive MOF films by linker functionalization

Sumea Klokic,<sup>a,b</sup> Benedetta Marmiroli,<sup>b</sup> Denys Naumenko,<sup>b</sup> Giovanni Birarda,<sup>c</sup> Simone Dal Zilio,<sup>d</sup> Miriam de J. Velásquez-Hernández,<sup>e</sup> Paolo Falcaro,<sup>e</sup> Lisa Vaccari<sup>c</sup> and Heinz Amenitsch <sup>\*b</sup>

- a. CERIC-ERIC, Elettra Sincrotrone Trieste – SAXS Beamline, S.S. 14, 163.5 km, Basovizza, Trieste 34149, Italy
- b. Institute of Inorganic Chemistry, Graz University of Technology, 8010 Graz, Austria, Email: [heinz.amentisch@tugraz.at](mailto:heinz.amentisch@tugraz.at)
- c. Elettra Sincrotrone Trieste – SISSI Bio Beamline, S.S. 14, 163.5 km, Basovizza, Trieste 34149, Italy
- d. IOM-CNR, Laboratorio TASC, S.S. 14, 163.5 km, Basovizza, Trieste 34149, Italy
- e. Institute of Physical and Theoretical Chemistry, Graz University of Technology, 8010 Graz, Austria.

## Author contributions

H. A., and S. K. conceived and designed the project. S. K. carried out most of the experimental work including the fabrication of the system and wrote the manuscript. D. N. and B. M. assisted with the data analysis and completed the GIWAXS measurements with S. K., G. B. and L.V. completed the ATR Fourier-transform infrared measurements. S. D.-Z. provided some starting materials and performed SEM imaging. M.-J. V.- H. and P. F. carried out the nitrogen adsorption measurements and aided in the data analysis and writing of the manuscript and ESI.

## Contents

<b>1. Table of contents</b> .....	3
<b>2. Experimental</b> .....	6
<b>3. Sample positioning</b> .....	8
<b>4. Characterization of CI-DMOF-1 films</b> .....	9
<b>4.1. Grazing incidence wide angle x-ray scattering (GIWAXS) experiments</b> .....	9
<b>4.2. Attenuated total reflectance (ATR) experiments</b> .....	10
<b>4.3. SEM characterization</b> .....	11
<b>4.4. Adsorption measurements with N<sub>2</sub></b> .....	11
<b>5. Characterization of CI-DMOF-1 films by GIWAXS</b> .....	12
<b>6. Azobenzene infiltration and loading level in CI-DMOF-1/AB<sub>90min</sub></b> .....	18
<b>7. Orientation analysis of the CI-DMOF-1 film</b> .....	24
<b>8. Characterization of bulk CI-DMOF-1</b> .....	25
<b>8.1. N<sub>2</sub>-Sorption characteristics of bulk CI-DMOF-1 and DMOF-1</b> .....	26
<b>9. Comparison of chemical and physical properties between CI-DMOF-1 and DMOF-1 (film, bulk)</b> .....	29

## 1. Table of contents

**Scheme S1 (a) SEM micrograph depicts a representative Cu(OH)<sub>2</sub> nanobelt film** which is the starting structure for the subsequent growth of the **CI-DMOF-1** films. Typically, upon deposition of Cu(OH)<sub>2</sub> nanobelts on a substrate, a preferential orientation is obtained with the long or short-axis of the nanobelts stacking parallel to each other, respectively, as already described in ref. [1]. Depending on the orientation of the substrate itself with respect to the X-ray beam during GIWAXS measurements, the **(b)** short axis of the nanobelt or, **(c)** the long-axis of the Cu(OH)<sub>2</sub> nanobelts is oriented perpendicular to the beam. The respective GIWAXS pattern differs slightly in the appearance owed to the difference in the Cu(OH)<sub>2</sub> nanobelt alignment. For the structures investigated herein, the samples for GIWAXS measurements were positioned with the nanobelts oriented on the glass substrate as depicted in **(b)**. 8

**Scheme S2.** Schematics of the GIWAXS experimental set-up combined with the laser light source operating at 343 nm and the LED light source with a wavelength of 450 nm. The MOF film was placed onto the sample stage positioned from the detector at a sample-to-detector distance (SD) to reach the required wide-angle q-range. Between the light sources (343 nm, 450 nm, X-rays (0.154 nm)), a spatial overlap was ensured to probe specifically the photo-stimulated position on the film sample. The samples were always positioned with the long axis of Cu(OH)<sub>2</sub> nanobelts parallel to the X-rays (see Scheme S1). To stimulate the sample, the 343 nm and 450 nm light sources were operated alternately. .... 9

**Scheme S3** UV-Vis calibration curve using known concentrations of trans-AB in Acetone. The UV-Vis data were collected on a Cary 60 spectrophotometer (Agilent technologies) in a 300-600 nm range using a quartz cell. For the calibration curve, the peak absorbance at 441 nm was recorded for the respective concentrations. Triplicate measurements were performed for every concentration ( $R^2 = 0.9992$ ). The extracted azobenzene from the CI-DMOF-1 powder employing acetone was accomplished after the extraction with acetone ( $A(441\text{ nm}) = 0.006$ ,  $c = 0.009\text{ mM}$ ; red square). The loading level for the bulk powder was determined with 0.47 molecules per pore. .... 19

**Figure S1 GIWAXS pattern of the films.** The **CI-DMOF-1** film structure shows a preferential orientation in the out-of-plane and in-plane direction. The cuts employed for data analysis for the out-of-plane (cut margin 40 pixels, red-dotted line) and in-plane (cut margin 5 pixels, red dotted line) are denoted by the black arrows. .... 12

**Figure S2** Top-view SEM images of the **CI-DMOF-1** film structures grown for **(a)** 10 min, **(b)** 30 min, **(c)** 60 min, **(d)** 90 min, **(e)** 180 min and **(f)** 270 min. These images display a different area on the respective films in contrast to those shown in Fig. 2 in the main manuscript to display the coverage of the films as well as the homogeneity of **CI-DMOF-1** crystallite growth on the lower Cu<sub>2</sub>bdc<sub>2</sub>-on-Cu(OH)<sub>2</sub> structure. .... 13

**Figure S3** GIWAXS integrated and 2D pattern of the **CI-DMOF-1** structure on oriented Cu<sub>2</sub>bdc<sub>2</sub>-on-Cu(OH)<sub>2</sub> films grown for **(a)** 10 min, **(b)** 30 min and **(c)** 60 min. The orientation of the films is deduced from the out-of-plane and in-plane cuts. Additionally, the indexing of the corresponding reflections for the P4/mmm (green) and I4/mcm (black) has been done according to ref.7. .... 14

**Figure S4** GIWAXS integrated and 2D pattern of the CI-DMOF-1 structure on oriented Cu<sub>2</sub>bdc<sub>2</sub>-on-Cu(OH)<sub>2</sub> films grown for **(a)** 90 min, **(b)** 180 min and **(c)** 270 min. The orientation of the films is deduced from the out-of-plane and in-plane cuts. Additionally, the indexing of the corresponding reflections for the P4/mmm (green) and I4/mcm (black) has been done according to ref. 7. .... 15

**Figure S5 Comparison of crystalline phases of the chloro-functionalized CI-DMOF-1 film grown (90 min).** **(a)** Out-of-plane integrated GIWAXS pattern of the (100) reflection for the **CI-DMOF-1** film and, **(b)** in-plane integrated GIWAXS pattern of the (001) reflection as a function of the rotation angle  $\phi$ . The film rotation was conducted between 0 – 275°. **(c)** Position of the (100) reflection as a function of the  $\phi$ -angle with respect to the presence of the P4/mmm phase denoted by  $q_{P4/mmm}$  and the I4/mcm phase given by  $q_{I4/mcm}$  (out-of-plane). The respective peak positions were extracted by fitting the (100) reflection. **(d)** Position of the characteristic (100), (001) reflections and (001)<sub>Cu<sub>2</sub>bdc<sub>2</sub></sub> at  $\phi = 0^\circ$  (mainly P4/mmm phase) and  $\phi = 154^\circ$  (mainly I4/mcm phase) are shown for the out-of-plane direction. **(e)** In-plane integrated GIWAXS pattern displaying the (001)<sub>Cu<sub>2</sub>bdc<sub>2</sub></sub> reflection of the Cu<sub>2</sub>bdc<sub>2</sub> substructure of the **CI-DMOF-1-on-Cu<sub>2</sub>bdc<sub>2</sub>-on-Cu(OH)<sub>2</sub>** film at different azimuthal angles with  $\phi = 0^\circ, 110^\circ$  and  $200^\circ$ .

The heteroepitaxially grown  $\text{Cu}_2\text{bdc}_2$  structure on  $\text{Cu}(\text{OH})_2$  nanobelts typically shows a strong azimuthal-angle dependence in the in-plane direction.<sup>[1]</sup> **(f)** The azimuthal angle dependence of the  $\text{Cu}_2\text{bdc}_2$  substructure was confirmed to persist after the growth of the upper **CI-DMOF-1** structure. **(g)** The position of the  $(001)_{\text{Cu}_2\text{bdc}_2}$  reflection as a function of azimuthal angle remains within a certain error around  $q = 5.8 \text{ nm}^{-1}$ . ..... 16

**Figure S6 (a)** ATR measurements of the pristine and azobenzene (AB) exposed **CI-DMOF-1**<sub>10min</sub> film grown for 10 min. The strong vibrational bands at  $1661 \text{ cm}^{-1}$  and  $1513 \text{ cm}^{-1}$  (indicated by asterisk), **(b)**, are attributed to the non-coordinated Cl-bdc or bdc linkers, which constitute to the upper **CI-DMOF-1** and lower  $\text{Cu}_2\text{bdc}_2$  structure, respectively. **(c)** Within the spectral resolution, the peak located at  $690 \text{ cm}^{-1}$  is attributed to the trans-azobenzene molecule. In comparison, the azobenzene-exposed **CI-DMOF-1**<sub>10min</sub> film structure in **(a)** shows a strong trans-azobenzene vibration which is similar to **(c)**. Accordingly, the azobenzene is expected in its relaxed, non-infiltrated state as the **CI-DMOF-1**<sub>10min</sub> structure has a poor growth as discussed in the main text. .... 20

**Figure S7** ATR measurements of the pristine and azobenzene (AB) infiltrated **CI-DMOF-1** films grown **(a)** 30 min and **(b)** 60 min. The successful growth of the structures is confirmed by the appearance of the characteristic C-O vibrational bands indicated by blue, which differ from those arising from the oriented  $\text{Cu}_2\text{bdc}_2$ -on- $\text{Cu}(\text{OH})_2$  substructure (grey dotted trace). The successful azobenzene infiltration is envisioned for the respective **CI-DMOF-1/AB** structures in the graphs on the right. .... 21

**Figure S8** ATR measurements of the pristine and azobenzene infiltrated **CI-DMOF-1** films grown for **(a)** 90 min, **(b)** 180 min and **(c)** 270 min. The successful growth of the structures is confirmed by the appearance of the characteristic C-O vibrational bands indicated by blue, which differ from those arising from the oriented  $\text{Cu}_2\text{bdc}_2$ -on- $\text{Cu}(\text{OH})_2$  substructure (grey dotted trace). The growth of the respective **CI-DMOF-1** is further seen since the vibrational bands corresponding to the asymmetric stretching of the carboxylic group ( $\nu_{\text{as}} = 1580 \text{ cm}^{-1}$ ) is shifted when compared to the substructure. The successful azobenzene infiltration is envisioned for the respective **CI-DMOF-1/AB** structures in the graphs on the right. .... 22

**Figure S9 Rigid CI-DMOF-1/AB structures.** **(a)** ATR spectra of the **CI-DMOF-1/AB**<sub>30min</sub> structure lacking the presence of azobenzene upon the attempt of the initial isomerization by light of 343 nm and 450 nm wavelength. **(b)** The **CI-DMOF-1/AB**<sub>60min</sub> structure comprises weak vibrational bands located around  $\nu_{\text{AB}} = 692 \text{ cm}^{-1}$  indicating the presence of azobenzene, yet, the changes between the ON and the OFF state are weak. .... 23

**Figure S10 Orientation analysis of the CI-DMOF-1 and CI-DMOF-1/AB film structure at 90 min.** **(a)** Magnified GIWAXS pattern of the **CI-DMOF-1** structure. The arrow is indicating the direction of azimuthal  $\chi$  integration where the vertical dashed line is at  $\chi = 0^\circ$ . Orientation analysis was performed for the two most intense reflections, (100) and (001) as indicated by the black frame. **(b)** Chi- $(\chi)$ -plots of the (100) reflection. Considering the isotropic contribution (grey shaded area), the calculated degree of orientation (DO) was determined according to ref. [2] with 49% ( $DO (\%) = \frac{A_{\text{total}} - A_{\text{isotropic}}}{A_{\text{total}}}$ ). **(c)** For the weak (001) reflection, only 9% were found to orient preferentially in the in-plane direction. **(d)** Orientation analysis was further performed for the azobenzene infiltrated **CI-DMOF-1/AB** structure for the two reflections, (100) and (001). **(e)** The degree of orientation for the (100) reflection was determined to decrease to 32%, owed to the increase of the isotropic contribution. **(f)** For the loaded structure, the (001) reflection was determined to orient with a slight preference in the in-plane direction which accounts for 9%. .... 24

**Figure S11** FT-IR characterisation of the bulk **CI-DMOF-1** system (purple trace, dried in vacuum). The C-Cl vibrations were allocated at  $791 \text{ cm}^{-1}$  and  $658 \text{ cm}^{-1}$ , based on the vibrations of the free  $\text{Cl}_2$ -bdc linker (yellow trace). The C-O vibrational band located at  $1650 \text{ cm}^{-1}$  is blue-shifted by  $14 \text{ cm}^{-1}$  compared to the non-functionalized DMOF-1 structure (grey trace), owed to the halogenated bdc-linker molecule. .... 25

**Figure S 12** Powder pattern of the bulk **CI-DMOF-1** system (purple trace) and for comparison, the non-functionalized pristine DMOF-1 system (grey trace). The prior is isostructural to the non-functionalized DMOF-1. .... 25

**Figure S13** N<sub>2</sub> sorption isotherms of **(a)** CI-DMOF-1 (purple) and DMOF-1 (grey). The marked area (I) is shown as a zoom-in on the region displaying a weak opening of the DMOF-1 pores upon N<sub>2</sub> adsorption. This behaviour is absent for CI-DMOF-1. **(b)** The adsorption and desorption branches are displayed as solid and open markers, respectively. **(c)** The calculated pore size distribution (DFT) for the respective structures is displayed with 8 Å DMOF-1 and 6 Å for CI-DMOF-1. .... 28

**Table S1 Parameters for the calculation of the azobenzene loading in CI-DMOF-1 films.**  $\Delta A$  denotes the  $\pi$ - $\pi^*$  band,  $\epsilon_{\text{cis-AB}}$  and  $\epsilon_{\text{trans-AB}}$  the extinction coefficients for the cis- and trans-isomers, respectively.  $\Delta X_{\text{AB}}$  refers to the change of the cis-content throughout the photo-switch and  $d_{\text{CI-DMOF-1 film}}$  to the film thickness of the **CI-DMOF-1/AB** crystallites oriented as the film system. .... 18

**Table S2** Vibrational bands of the **CI-DMOF-1** and **CI-DMOF-1/AB** structures grown at different times. Here,  $\nu_{\text{AB}}$  denotes the C-H bending mode of azobenzene,<sup>5c</sup> while  $\nu_s$  and  $\nu_{\text{as}}$  are attributed to the symmetric and asymmetric stretching, respectively, of the carboxylic group from the Cl<sub>2</sub>-bdc linker coordinated to the zinc metal. .... 23

**Table S3** Comparison of the DMOF-1 film structure reported in ref. 2 and the herein investigated CI-DMOF-1 film structure. .... 29

## 2. Experimental

### Materials and methods

All chemicals and solvents are available commercially and were used as received without any further purification. Experiments were performed at ambient pressure and the products are stable at ambient conditions.

### Preparation of linker functionalized CI-DMOF-1 films

In the first step, copper hydroxide nanobelts were deposited on sodalime glass substrates following the automated deposition procedure.<sup>[1]</sup> Details regarding the fabrication process and  $\text{Cu}_2\text{bdc}_2$  growth can be found elsewhere.<sup>[2]</sup> The films were subsequently converted for 60 min in 10 mL of an ethanolic  $\text{Zn}(\text{acetate})_2$  dihydrate solution (2.2 mg). After gentle washing by ethanol, the zinc-functionalized films were immersed in 10 mL of a methanolic solution containing the linkers *dabco* (4.8 mg, 1,4-diazabicyclo[2.2.2]octan) and  $\text{Cl}_2\text{-bdc}$  (7.2 mg, 2,5-dichloroterephthalic acid) to yield the **CI-DMOF-1**. The conversion to the functionalized structures was accomplished at 60°C for growth times of 10 min, 30 min, 60 min, 90 min, 180 min and 270 min. According to the isorecticular design principle, we kept the molar ratio of the two linker molecule equal to the DMOF-1 film fabrication protocol ( $n_{\text{BDC}}:n_{\text{DMOF-1}}=1$ ).<sup>[2]</sup>

### Azobenzene infiltration process

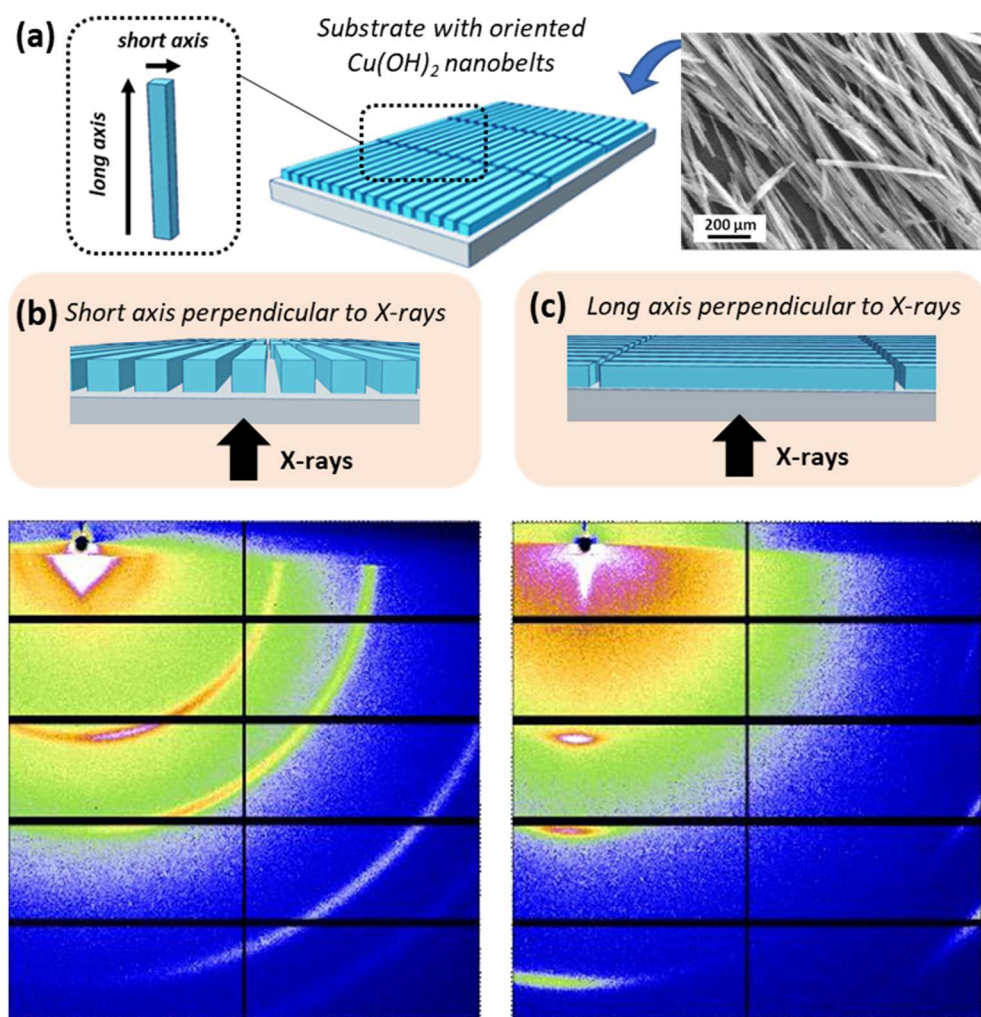
The pristine **CI-DMOF-1** film structures were activated for 15 min at 60°C prior to the infiltration process. The azobenzene incorporation was conducted according to the vapor assisted procedure reported in ref. [2], using 60  $\mu\text{L}$  of a 10 mg/mL acetic azobenzene solution. The process was accomplished within one hour at 60°C.

### Preparation of bulk CI-DMOF-1

The preparation of the DMOF-1 MOF powder was adapted from the procedure reported elsewhere.<sup>[6a]</sup> Briefly, 2.0 g zinc(II) nitrate hexahydrate was mixed with 1.02 g 2,5-dichloroterephthalic acid ( $\text{Cl}_2\text{-bdc}$ ) in 40 mL DMF upon dissolution of the solids at 100°C. Subsequently, 0.38 g 1,4-diazabicyclo[2.2.2]octan (*dabco*) was added and the reaction was

stirred for 24 h under refluxing conditions yielding a colorless precipitate, which was filtered in vacuo. The colorless powdery precipitate was dried under vacuum for 3 h at 120°C yielding Cl-DMOF-1 (0.50 g). The system was characterized by FT-IR (Figure S11) and XRD (Figure S 12).

### 3. Sample positioning



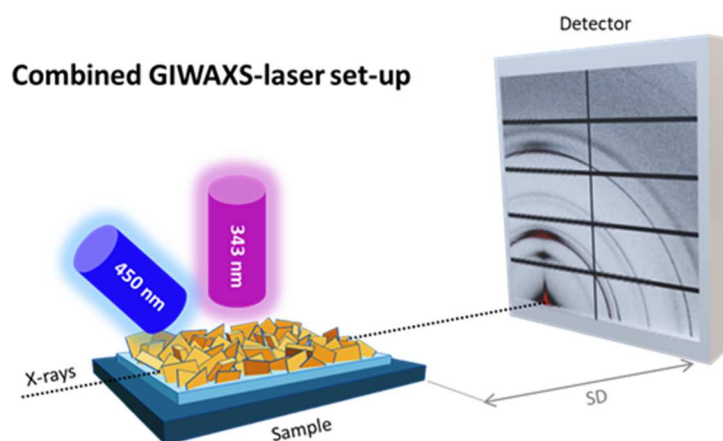
**Scheme S1 (a)** SEM micrograph depicts a representative  $\text{Cu}(\text{OH})_2$  nanobelt film which is the starting structure for the subsequent growth of the **CI-DMOF-1** films. Typically, upon deposition of  $\text{Cu}(\text{OH})_2$  nanobelts on a substrate, a preferential orientation is obtained with the long or short-axis of the nanobelts stacking parallel to each other, respectively, as already described in ref. [1]. Depending on the orientation of the substrate itself with respect to the X-ray beam during GIWAXS measurements, the **(b)** short axis of the nanobelt or, **(c)** the long-axis of the  $\text{Cu}(\text{OH})_2$  nanobelts is oriented perpendicular to the beam. The respective GIWAXS pattern differs slightly in the appearance owed to the difference in the  $\text{Cu}(\text{OH})_2$  nanobelt alignment. For the structures investigated herein, the samples for GIWAXS measurements were positioned with the nanobelts oriented on the glass substrate as depicted in **(b)**.



## 4. Characterization of CI-DMOF-1 films

### 4.1. Grazing incidence wide angle x-ray scattering (GIWAXS) experiments

Static GIWAXS measurements of the **CI-DMOF-1** structures prior and upon their infiltration by azobenzene were performed at the Austrian SAXS beamline at ELETTRA, Trieste, Italy,<sup>[3]</sup> with the access granted by the CERIC-ERIC consortium (Proposal No. 20212195, 20222149). Measurements were conducted at a sample to detector distance of 518 mm providing a  $q$ -range from  $0.08 < q < 17 \text{ nm}^{-1}$ , where  $q$  denotes the length of the scattering vector ( $q = \frac{4\pi}{\lambda} \sin\left(\frac{2\theta}{2}\right)$ ),  $\lambda$  being the wavelength (0.154 nm, 8 keV) and  $\theta$  the scattering angle; see Scheme S2. The beam size was 1.0 x 0.2 mm (h x v), and the 2D GIWAXS patterns were acquired for 60 s at an incident grazing angle of 0.2°.



**Scheme S2.** Schematics of the GIWAXS experimental set-up combined with the laser light source operating at 343 nm and the LED light source with a wavelength of 450 nm. The MOF film was placed onto the sample stage positioned from the detector at a sample-to-detector distance (SD) to reach the required wide-angle  $q$ -range. Between the light sources (343 nm, 450 nm, X-rays (0.154 nm)), a spatial overlap was ensured to probe specifically the photo-stimulated position on the film sample. The samples were always positioned with the long axis of  $\text{Cu}(\text{OH})_2$  nanobelts parallel to the X-rays (see Scheme S1). To stimulate the sample, the 343 nm and 450 nm light sources were operated alternately.

For the photo-excitation experiments, GIWAXS patterns were acquired for 0.99 s due to the fast structural transformation of the **CI-DMOF-1** films. For this, a Pilatus3 1M detector was used (Dectris Ltd, Baden Switzerland with an active area of 169 x 179 mm<sup>2</sup> and a pixel size of 172 μm), and the images were processed by SAXSDOG.<sup>[4]</sup> For data analysis, a vertical cut in the out-of-plane direction and a horizontal cut in the in-plane direction were considered, as well as radial integration of the GIWAXS pattern (Figure S1). The integrated GIWAXS patterns were processed using Igor pro (Wavemetrics, Inc., Lake Oswego, OR). The protocol for the photo-excitation experiments was elaborated earlier with details provided in ref. [2]. The laser power (femtosecond laser, Yb:KGW, PHAROS) for the 343 nm light source was chosen throughout the experiments with 8090 mW (RA 25 A) with a power density at the sample plane of 130 mW cm<sup>-2</sup>. The films were converted to the relaxed state by using light with a wavelength of 450 nm (PL450B, OSRAM Opto Semiconductors) with a power density of 17.2 mW cm<sup>-2</sup> throughout the experiments. The photo-switching experiment to deduce the time constant were repeated six times.

#### **4.2. Attenuated total reflectance (ATR) experiments**

Infrared measurements of the pristine and infiltrated **CI-DMOF-1** film systems were acquired at SISSI-Bio offline end station of the SISSI beamline at Elettra Sincrotrone Trieste, with the access granted by the CERIC-ERIC consortium (Proposal No. 20212195, 20222149).<sup>[5]</sup> For both, static and time-resolved measurements, an interferometer was used (VERTEX 70, Bruker Optics, MA, US), equipped with a DTGS detector and an ATR diamond accessory (MIRACLE, Pike Optics). Prior the measurement, a reference was collected on the clean crystal, then a spectrum of the sample was recorded averaging 128 scans at 10 kHz scanner speed, with a spectral resolution of 1 cm<sup>-1</sup> with a zero filling of 2 before the FFT.

### **4.3. SEM characterization**

Morphologies of samples were observed by a scanning electron microscope (Field Emission Scanning Electron Microscope Gemini Column (FEG) ZEISS SIGMA 300; WD = 7.1 mm; acceleration voltage 3.00 kV).

### **4.4. Adsorption measurements with N<sub>2</sub>**

The gas sorption properties of activated samples of DMOF-1 (0.1045 g) and Cl-DMOF-1 (0.083 g) were studied through N<sub>2</sub> physisorption experiments. Both materials were degassed under vacuum at 393 K for 12 h. Then, N<sub>2</sub> adsorption-desorption isotherms were recorded at 77 K using a Micromeritics 3FLEX instrument, and He was used for free space determination. The collected data indicates that both, DMOF-1 and Cl-DMOF-1, exhibit a type-I N<sub>2</sub> physisorption isotherms, indicating the presence of micropores (Figure S13, a). The surface area was calculated using the Brunauer-Emmett-Teller (BET) method using the Rouquerol consistency criteria suggested in the literature.<sup>[6]</sup>

## 5. Characterization of CI-DMOF-1 films by GIWAXS

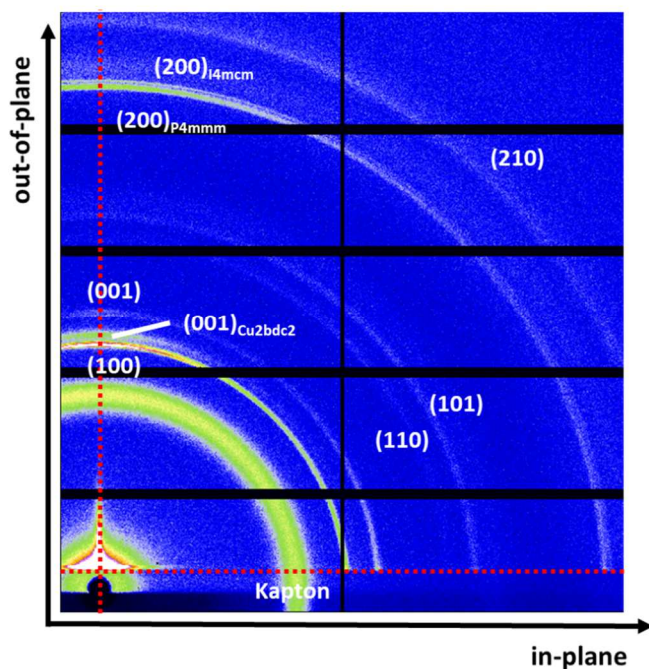


**Figure S1** GIWAXS pattern of the films. The CI-DMOF-1 film structure shows a preferential orientation in the out-of-plane and in-plane direction. The cuts employed for data analysis for the out-of-plane (cut margin 40 pixels, red-dotted line) and in-plane (cut margin 5 pixels, red dotted line) are denoted by the black arrows.

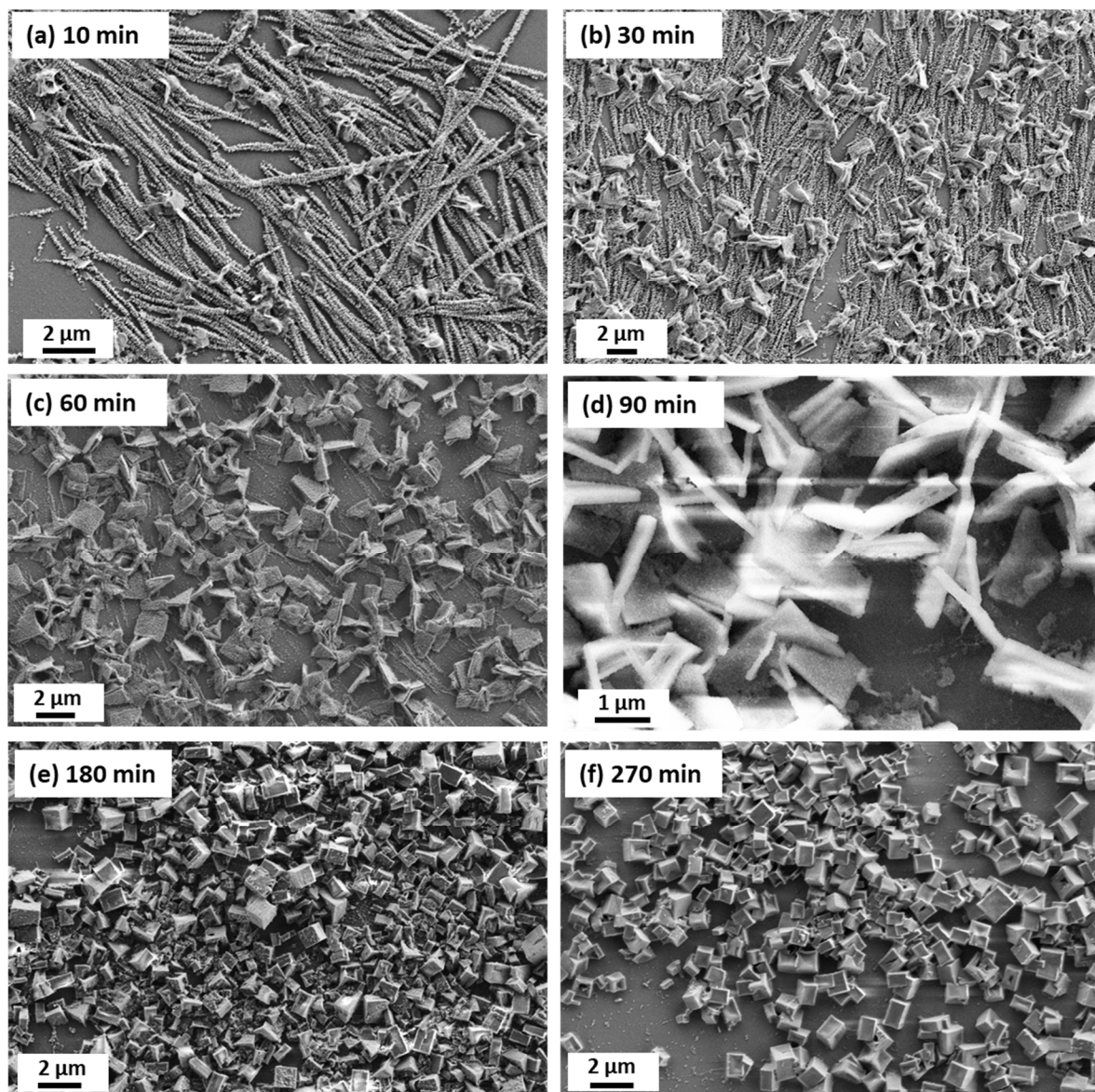


**Figure S2** Top-view SEM images of the **CI-DMOF-1** film structures grown for **(a)** 10 min, **(b)** 30 min, **(c)** 60 min, **(d)** 90 min, **(e)** 180 min and **(f)** 270 min. These images display a different area on the respective films in contrast to those shown in Fig. 2 in the main manuscript to display the coverage of the films as well as the homogeneity of **CI-DMOF-1** crystallite growth on the lower  $\text{Cu}_2\text{btc}_2\text{-on-Cu(OH)}_2$  structure.



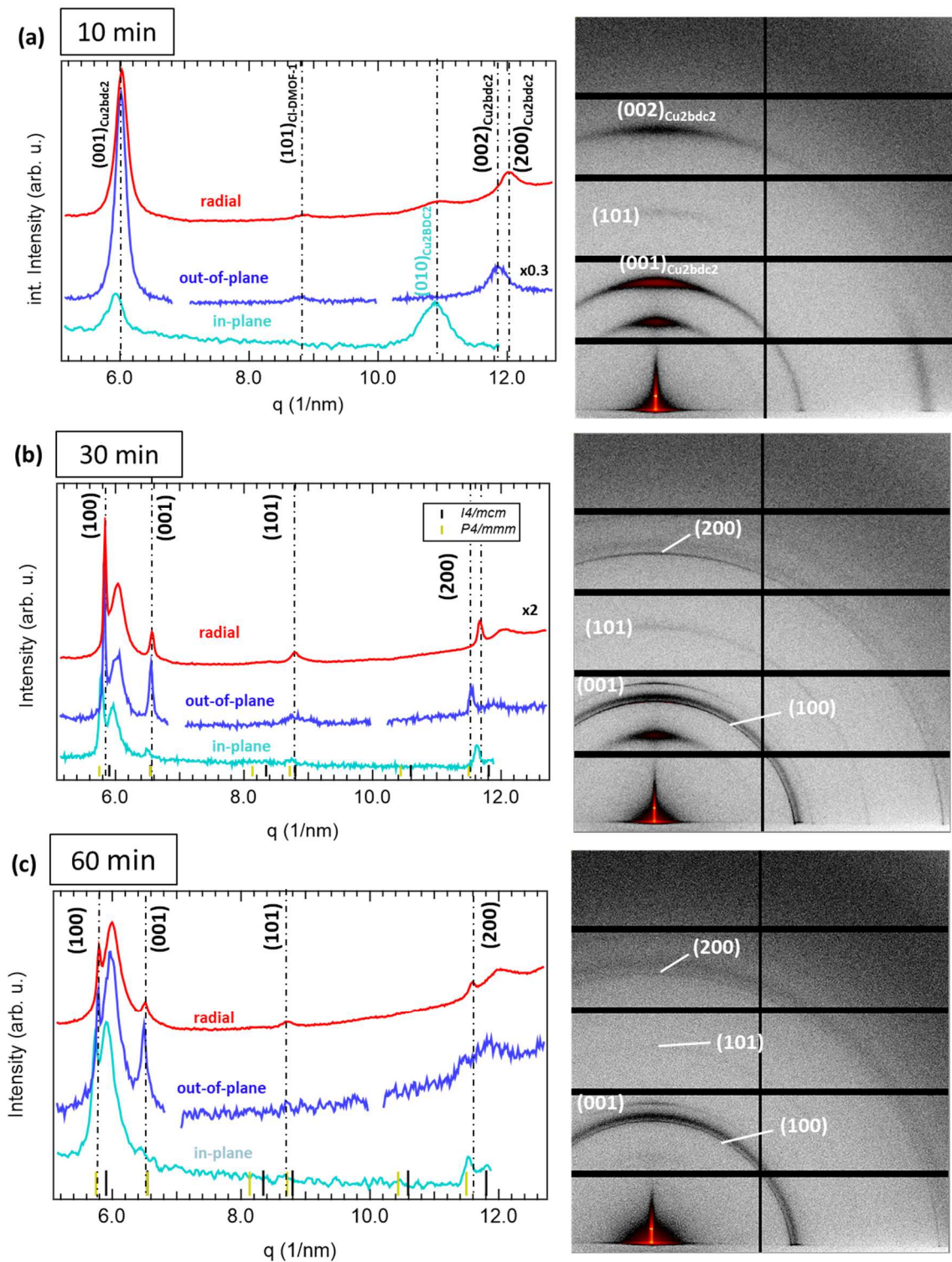


**Figure S3** GIWAXS integrated and 2D pattern of the **CI-DMOF-1** structure on oriented  $\text{Cu}_2\text{bdc}_2$ -on- $\text{Cu}(\text{OH})_2$  films grown for **(a)** 10 min, **(b)** 30 min and **(c)** 60 min. The orientation of the films is deduced from the out-of-plane and in-plane cuts. Additionally, the indexing of the corresponding reflections for the  $P4/mmm$  (green) and  $I4/mcm$  (black) has been done according to ref.7.

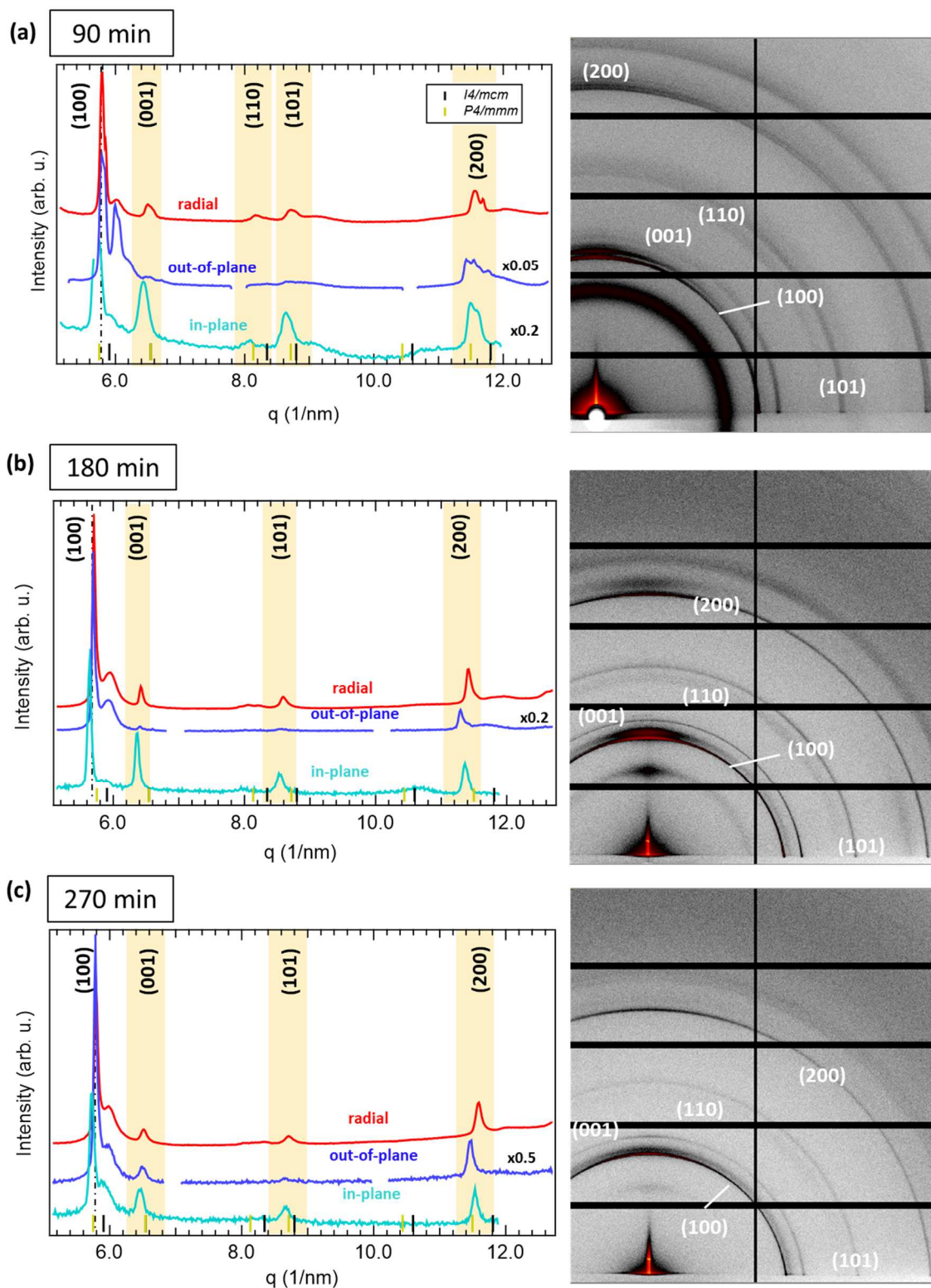


**Figure S4** GIWAXS integrated and 2D pattern of the CI-DMOF-1 structure on oriented  $\text{Cu}_2\text{bdc}_2\text{-on-Cu(OH)}_2$  films grown for (a) 90 min, (b) 180 min and (c) 270 min. The orientation of the films is deduced from the out-of-plane and in-plane cuts. Additionally, the indexing of the corresponding reflections for the  $P4/mmm$  (green) and  $I4/mcm$  (black) has been done according to ref. 7.



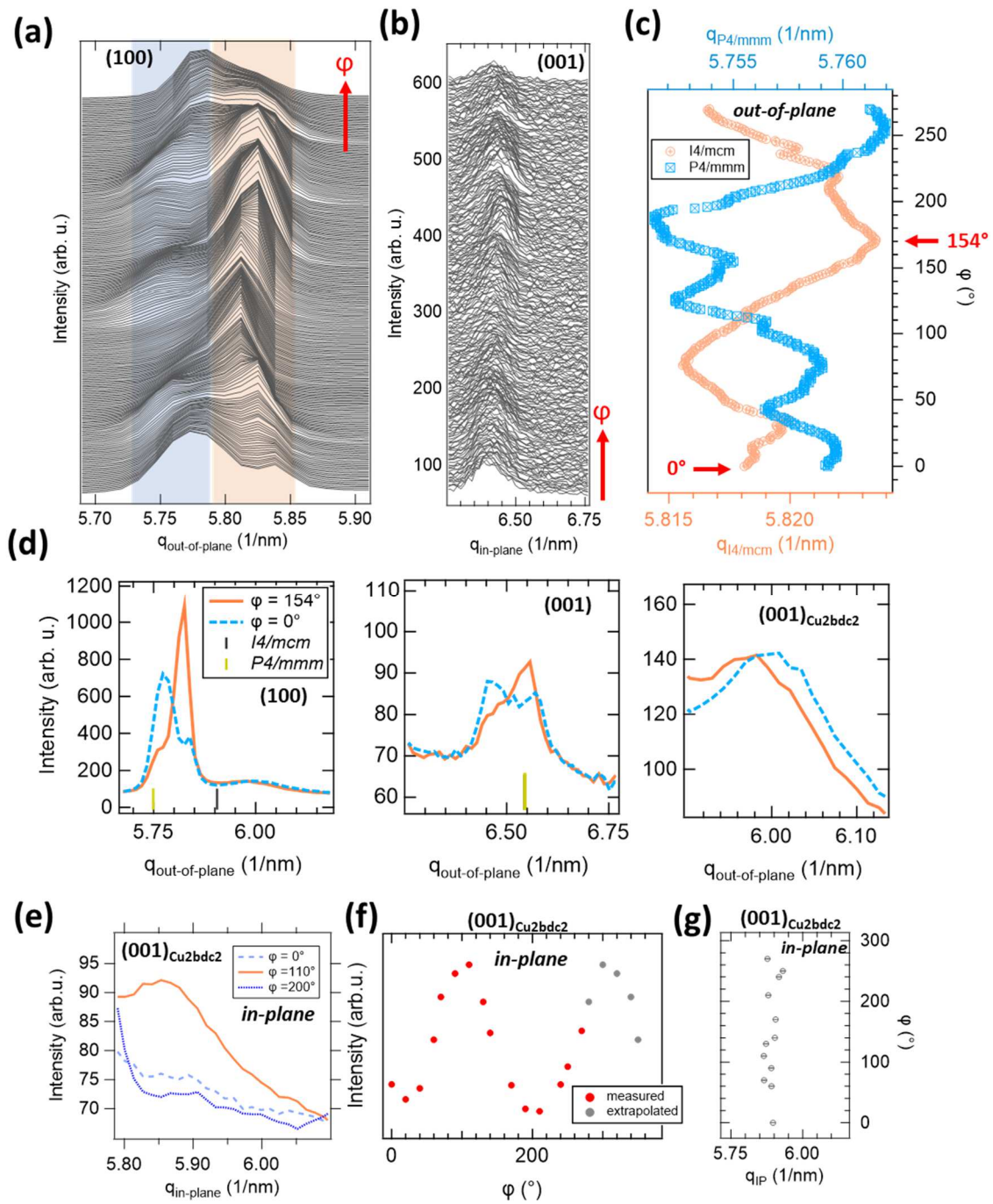


**Figure S5 Comparison of crystalline phases of the chloro-functionalized CI-DMOF-1 film grown (90 min).** (a) Out-of-plane integrated GIWAXS pattern of the (100) reflection for the CI-DMOF-1 film and, (b) in-plane integrated GIWAXS pattern of the (001) reflection as a function of the rotation angle  $\phi$ . The film rotation was conducted between 0 – 275°. (c) Position of the (100) reflection as a function of the  $\phi$ -angle with respect to the presence of the  $P4/mmm$  phase denoted by  $q_{P4/mmm}$  and the  $I4/mcm$  phase given by  $q_{I4/mcm}$  (out-of-plane). The respective peak positions were extracted by fitting the (100) reflection. (d) Position of the characteristic (100),



(001) reflections and  $(001)_{\text{Cu}_2\text{bdc}_2}$  at  $\varphi = 0^\circ$  (mainly  $P4/mmm$  phase) and  $\varphi = 154^\circ$  (mainly  $I4/mcm$  phase) are shown for the out-of-plane direction. **(e)** In-plane integrated GIWAXS pattern displaying the  $(001)_{\text{Cu}_2\text{bdc}_2}$  reflection of the  $\text{Cu}_2\text{bdc}_2$  substructure of the **CI-DMOF-1-on- $\text{Cu}_2\text{bdc}_2$ -on- $\text{Cu}(\text{OH})_2$**  film at different azimuthal angles with  $\varphi = 0^\circ, 110^\circ$  and  $200^\circ$ . The heteroepitaxially grown  $\text{Cu}_2\text{bdc}_2$  structure on  $\text{Cu}(\text{OH})_2$  nanobelts typically shows a strong azimuthal-angle dependence in the in-plane direction.<sup>[1]</sup> **(f)** The azimuthal angle dependence of the  $\text{Cu}_2\text{bdc}_2$  substructure was confirmed to persist after the growth of the upper **CI-DMOF-1** structure. **(g)** The position of the  $(001)_{\text{Cu}_2\text{bdc}_2}$  reflection as a function of azimuthal angle remains within a certain error around  $q = 5.8 \text{ nm}^{-1}$ .

## 6. Azobenzene infiltration and loading level in CI-DMOF-1/AB<sub>90min</sub>

The loading level of azobenzene molecules per CI-DMOF-1 pore was calculated following the procedure reported in references 2 and 8.

Briefly, the loading level is calculated according to Eq. S1 and Eq. S2, with parameters summarized in

Table S1. Owing to the broad crystallite size distribution, the azobenzene loading level is given in a range, respectively.

$$\text{Loading} = c_{AB} * N_A * V_{CI-DMOF-1} = 0.5 \text{ to } 0.2 \frac{\text{molecules}}{\text{pore}} \quad \text{Eq. S1}$$

$$c_{AB} = \frac{\Delta A}{(\epsilon_{cis-AB} - \epsilon_{trans-AB}) * d_{CI-DMOF-1 \text{ film}} * \Delta x_{AB}} = 0.11 \text{ to } 0.28 \frac{\text{mol}}{\text{L}} \quad \text{Eq. S2}$$

**Table S1 Parameters for the calculation of the azobenzene loading in CI-DMOF-1 films.**

$\Delta A$  denotes the  $\pi$ - $\pi^*$  band,  $\epsilon_{cis-AB}$  and  $\epsilon_{trans-AB}$  the extinction coefficients for the *cis*- and *trans*-isomers, respectively.  $\Delta x_{AB}$  refers to the change of the *cis*-content throughout the photo-switch and  $d_{CI-DMOF-1 \text{ film}}$  to the film thickness of the **CI-DMOF-1/AB** crystallites oriented as the film system.

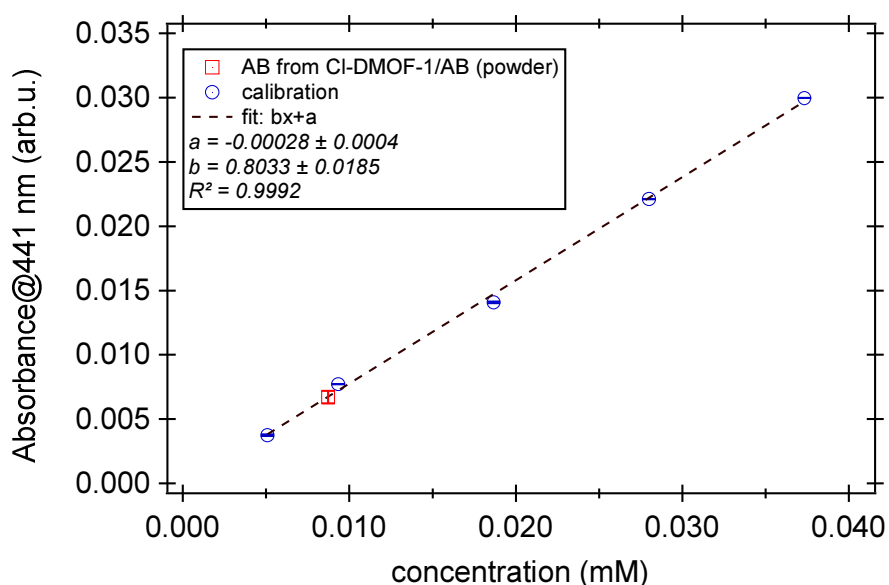
$\Delta A$ ( $\lambda = 330\text{nm}$ )	-0.2
$\epsilon_{cis-AB}$	2 500 L/mol cm <sup>[8]</sup>
$\epsilon_{trans-AB}$	22 000 L/mol cm <sup>[8]</sup>
$\Delta x_{AB}$ <sup>a</sup>	0.6
Thickness $d_{CI-DMOF-1 \text{ film}}$ <sup>b</sup>	2.0 - 0.8 $\mu\text{m}$
$V_{CI-DMOF-1/AB}$ <sup>c</sup>	2395 $\text{\AA}^3$
<b>Loading level</b>	<b>0.5 – 0.2 molecules/pore</b>

<sup>a</sup> Considering the second switching cycle

<sup>b</sup> The size of the crystallites was evaluated by ImageJ<sup>®</sup> displaying sizes in the denoted range. This parameter will influence the calculated loading level.

<sup>c</sup> Lattice parameters were estimated from the powder pattern of CI-DMOF-1/AB<sub>90min</sub>

Notably, the azobenzene loading level is much lower for the **CI-DMOF-1**<sub>90min</sub> film compared to the non-functionalized DMOF-1 film system (90 min growth time), where a loading level of 1 molecule per pore was reported.<sup>[2]</sup> In order to determine whether this difference arises from the chlorine substituents, the azobenzene loading of the respective bulk powders was determined (see SI chapter 8) following the procedure reported by Griffiths *et al.*<sup>[7b]</sup> By employing a calibration curve of known amounts of azobenzene in acetone, the loading level was calculated with 0.43 azobenzene molecules per CI-DMOF-1 pore using a sample amount of 5.3 mg. This value is in good agreement to the one obtained for the **CI-DMOF-1**<sub>90min</sub> film structure and indicates that the chemical functionalization alters the degree of azobenzene uptake.



**Scheme S3** UV-Vis calibration curve using known concentrations of *trans*-AB in Acetone. The UV-Vis data were collected on a Cary 60 spectrophotometer (Agilent technologies) in a 300-600 nm range using a quartz cell. For the calibration curve, the peak absorbance at 441 nm was recorded for the respective concentrations. Triplicate measurements were performed for every concentration ( $R^2 = 0.9992$ ). The extracted azobenzene from the CI-DMOF-1 powder employing acetone was accomplished after the extraction with acetone ( $A(441\text{ nm}) = 0.006$ ,  $c = 0.009\text{ mM}$ ; *red square*). The loading level for the bulk powder was determined with 0.47 molecules per pore.

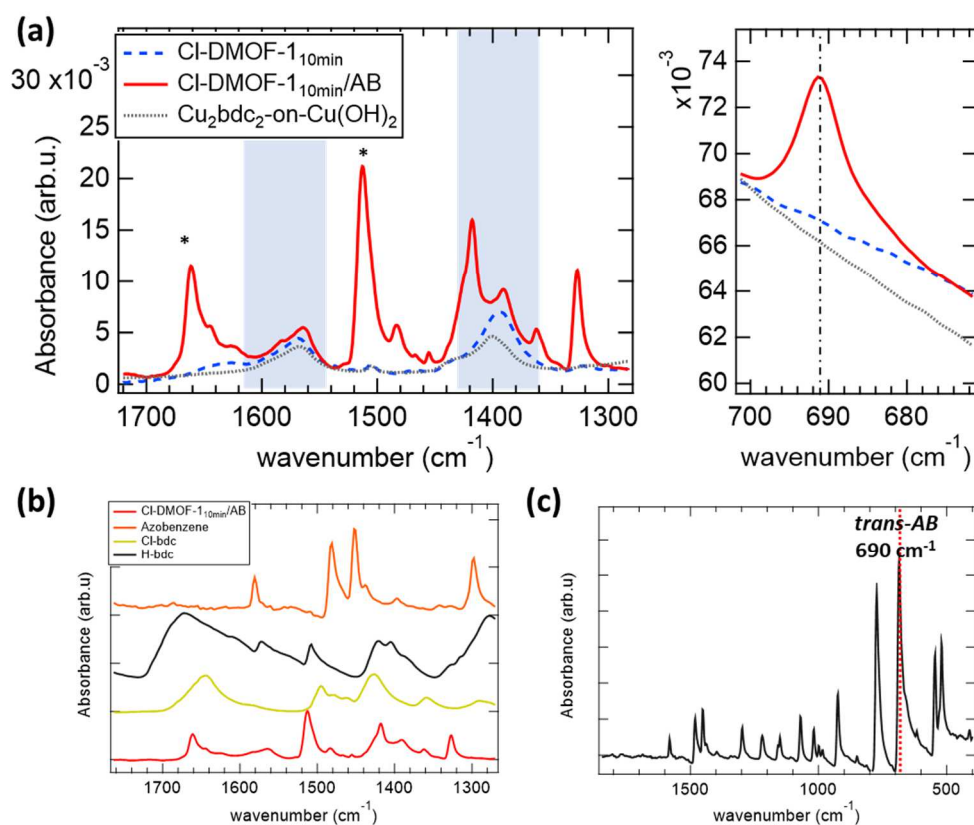


**Figure S6 (a)** ATR measurements of the pristine and azobenzene (AB) exposed **CI-DMOF-1<sub>10min</sub>** film grown for 10 min. The strong vibrational bands at 1661  $\text{cm}^{-1}$  and 1513  $\text{cm}^{-1}$  (indicated by asterisk), **b**, are attributed to the non-coordinated CI-bdc or bdc linkers, which constitute to the upper **CI-DMOF-1** and lower  $\text{Cu}_2\text{bdc}_2$  structure, respectively. **(c)** Within the spectral resolution, the peak located at 690  $\text{cm}^{-1}$  is attributed to the *trans*-azobenzene molecule. In comparison, the azobenzene-exposed **CI-DMOF-1<sub>10min</sub>** film structure in **(a)** shows a strong *trans*-azobenzene vibration which is similar to **(c)**. Accordingly, the azobenzene is expected in its relaxed, non-infiltrated state as the **CI-DMOF-1<sub>10min</sub>** structure has a poor growth as discussed in the main text.

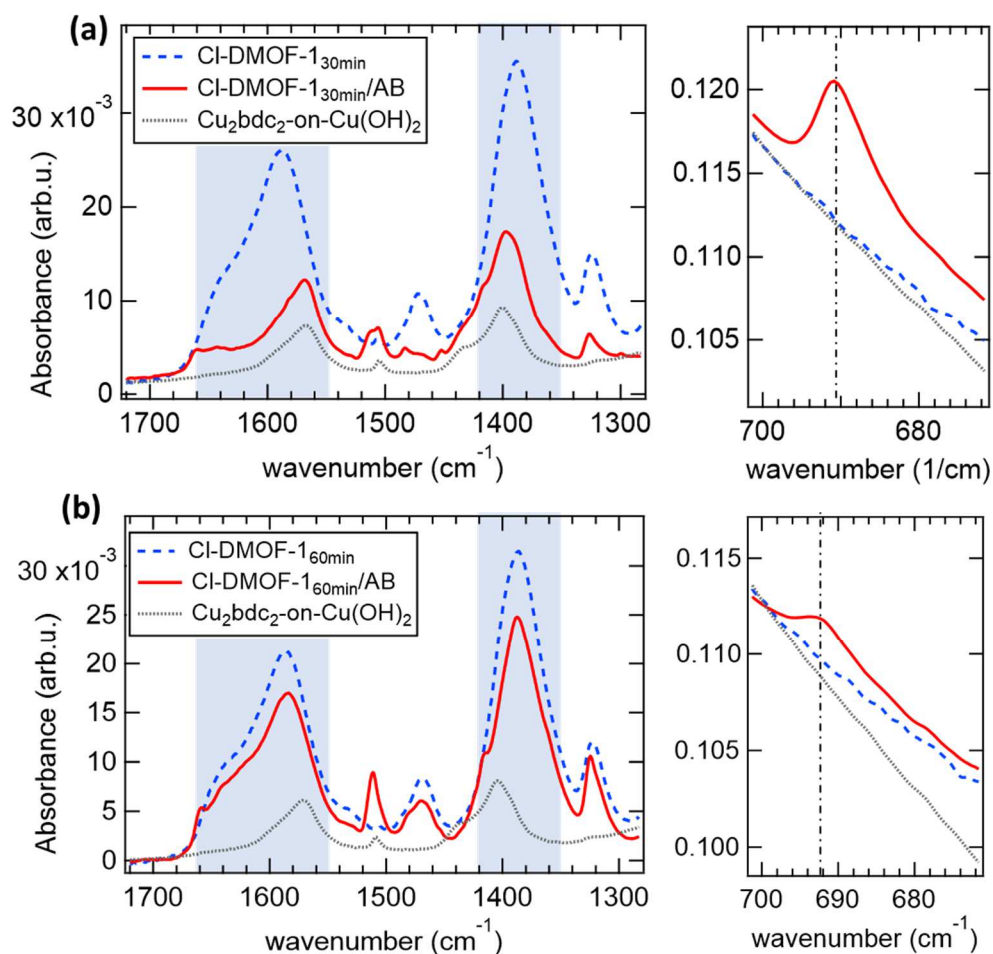


**Figure S7** ATR measurements of the pristine and azobenzene (AB) infiltrated **CI-DMOF-1** films grown **(a)** 30 min and **(b)** 60 min. The successful growth of the structures is confirmed by the appearance of the characteristic C-O vibrational bands indicated by blue, which differ from those arising from the oriented  $\text{Cu}_2\text{bdc}_2\text{-on-Cu(OH)}_2$  substructure (grey dotted trace). The successful azobenzene infiltration is envisioned for the respective **CI-DMOF-1/AB** structures in the graphs on the right.

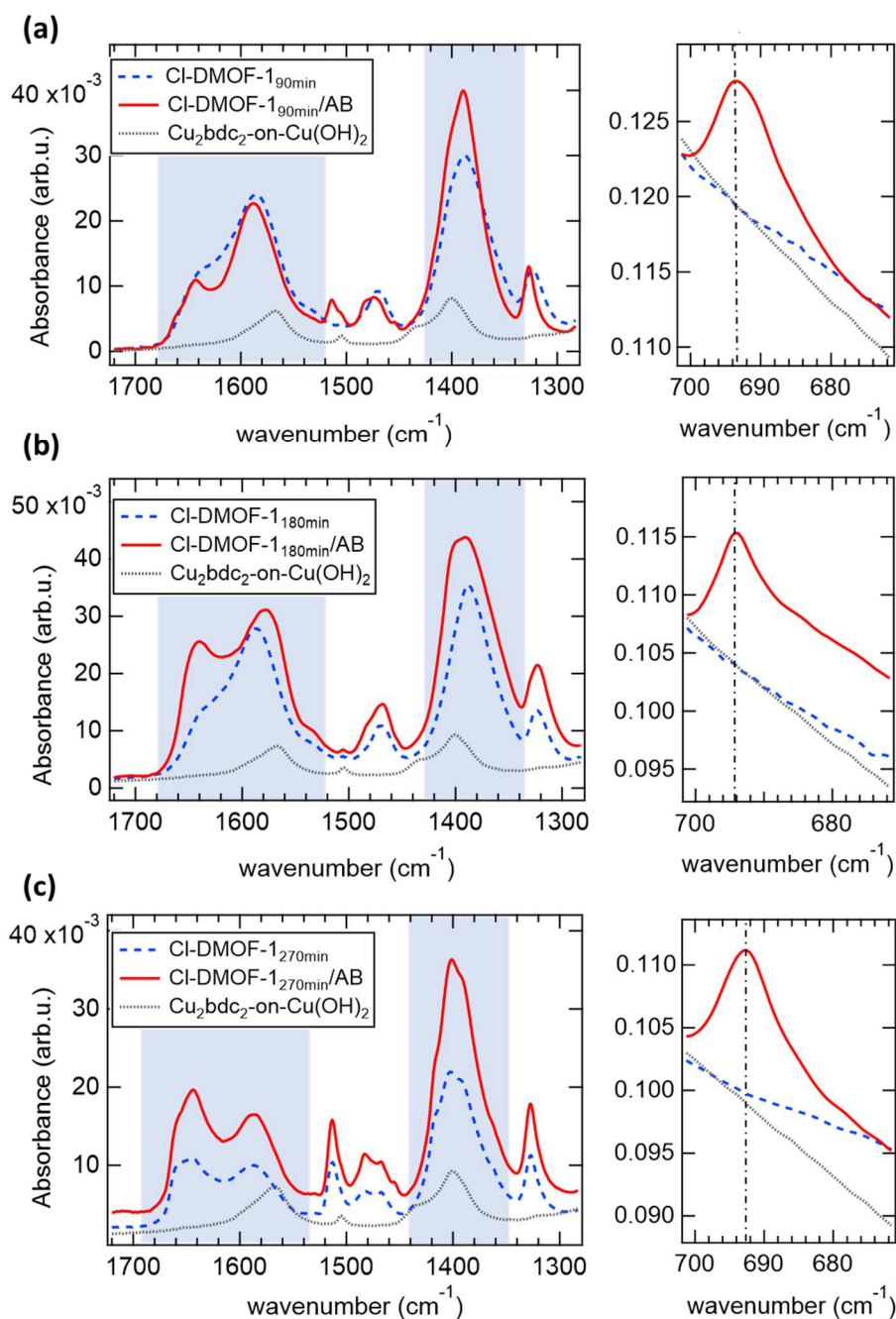


**Figure S8** ATR measurements of the pristine and azobenzene infiltrated **CI-DMOF-1** films grown for **(a)** 90 min, **(b)** 180 min and **(c)** 270 min. The successful growth of the structures is confirmed by the appearance of the characteristic C-O vibrational bands indicated by blue, which differ from those arising from the oriented  $\text{Cu}_2\text{bdc}_2\text{-on-Cu(OH)}_2$  substructure (grey dotted trace). The growth of the respective **CI-DMOF-1** is further seen since the vibrational bands corresponding to the asymmetric stretching of the carboxylic group ( $\nu_{as} = 1580 \text{ cm}^{-1}$ ) is shifted when compared to the substructure. The successful azobenzene infiltration is envisioned for the respective **CI-DMOF-1/AB** structures in the graphs on the right.

**Table S2** Vibrational bands of the **CI-DMOF-1** and **CI-DMOF-1/AB** structures grown at different times. Here,  $\nu_{AB}$  denotes the C-H bending mode of azobenzene,<sup>5c</sup> while  $\nu_s$  and  $\nu_{as}$  are attributed to the symmetric and asymmetric stretching, respectively, of the carboxylic group from the Cl<sub>2</sub>-bdc linker coordinated to the zinc metal.

t (min)	AB	CI-DMOF-1		CI-DMOF-1/AB	
	$\nu_{AB}$ (cm <sup>-1</sup> )	$\nu_s$ (cm <sup>-1</sup> )	$\nu_{as}$ (cm <sup>-1</sup> )	$\nu_s$ (cm <sup>-1</sup> )	$\nu_{as}$ (cm <sup>-1</sup> )
10	690	1393	1567	1390	1564
30	691	1387	1586	1397	1568
60	692	1388	1587	1389	1586
90	693	1388	1585	1389	1587 + 1643
180	694	1388	1587	1393	1578 + 1640
270	691	1402	1587 + 1644	1401	1587 + 1644

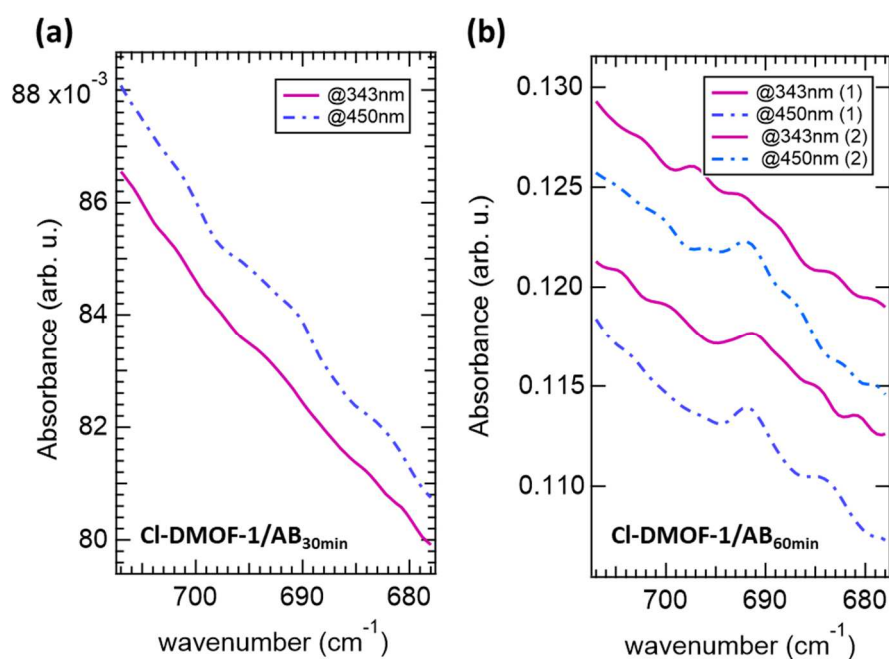


**Figure S9 Rigid CI-DMOF-1/AB structures.** (a) ATR spectra of the **CI-DMOF-1/AB<sub>30min</sub>** structure lacking the presence of azobenzene upon the attempt of the initial isomerization by light of 343 nm and 450 nm wavelength. (b) The **CI-DMOF-1/AB<sub>60min</sub>** structure comprises weak vibrational bands located around  $\nu_{AB} = 692$  cm<sup>-1</sup> indicating the presence of azobenzene, yet, the changes between the ON and the OFF state are weak.

## 7. Orientation analysis of the CI-DMOF-1 film

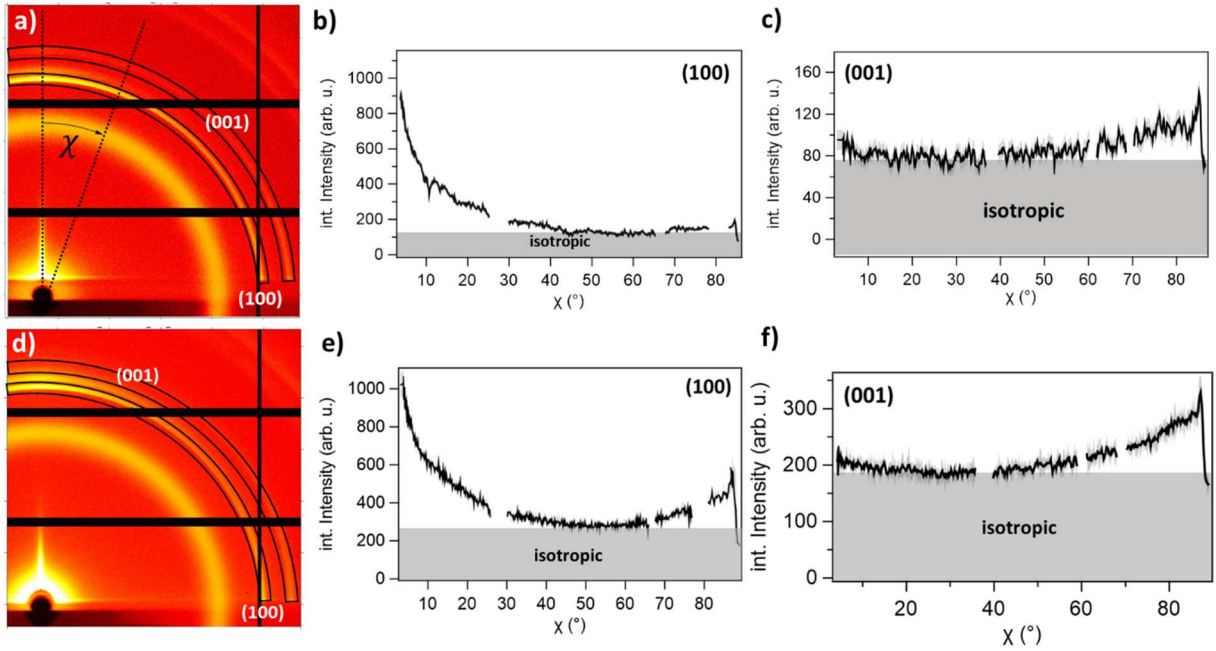


**Figure S10 Orientation analysis of the CI-DMOF-1 and CI-DMOF-1/AB film structure at 90 min.** (a) Magnified GIWAXS pattern of the **CI-DMOF-1** structure. The arrow is indicating the direction of azimuthal  $\chi$  integration where the vertical dashed line is at  $\chi = 0^\circ$ . Orientation analysis was performed for the two most intense reflections, (100) and (001) as indicated by the black frame. (b) Chi- $(\chi)$ -plots of the (100) reflection. Considering the isotropic contribution (grey shaded area), the calculated degree of orientation (DO) was determined according to ref. [2] with 49% ( $DO (\%) = \frac{Area_{total} - Area_{isotropic}}{Area_{total}}$ ). (c) For the weak (001) reflection, only 9% were found to orient preferentially in the in-plane direction. (d) Orientation analysis was further performed for the azobenzene infiltrated **CI-DMOF-1/AB** structure for the two reflections, (100) and (001). (e) The degree of orientation for the (100) reflection was determined to decrease to 32%, owed to the increase of the isotropic contribution. (f) For the loaded structure, the (001) reflection was determined to orient with a slight preference in the in-plane direction which accounts for 9%.



## 8. Characterization of bulk CI-DMOF-1

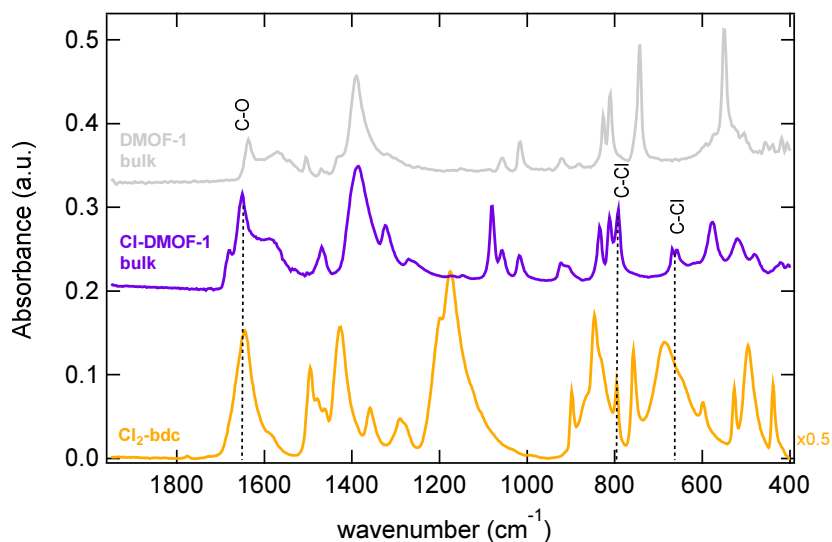


**Figure S11** FT-IR characterisation of the bulk CI-DMOF-1 system (purple trace, dried in vacuum). The C-Cl vibrations were allocated at  $791\text{ cm}^{-1}$  and  $658\text{ cm}^{-1}$ , based on the vibrations of the free  $\text{Cl}_2$ -bdc linker (yellow trace). The C-O vibrational band located at  $1650\text{ cm}^{-1}$  is blue-shifted by  $14\text{ cm}^{-1}$  compared to the non-functionalized DMOF-1 structure (grey trace), owed to the halogenated bdc-linker molecule.

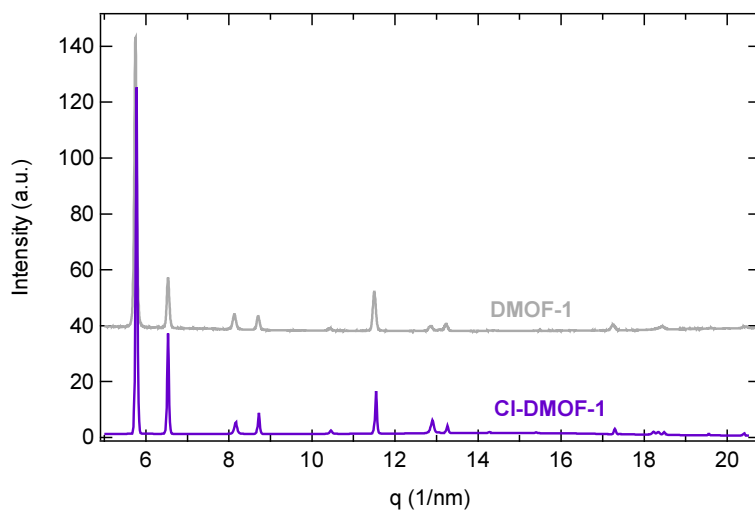


**Figure S 12** Powder pattern of the bulk CI-DMOF-1 system (purple trace) and for comparison, the non-functionalized pristine DMOF-1 system (grey trace). The prior is isostructural to the non-functionalized DMOF-1.

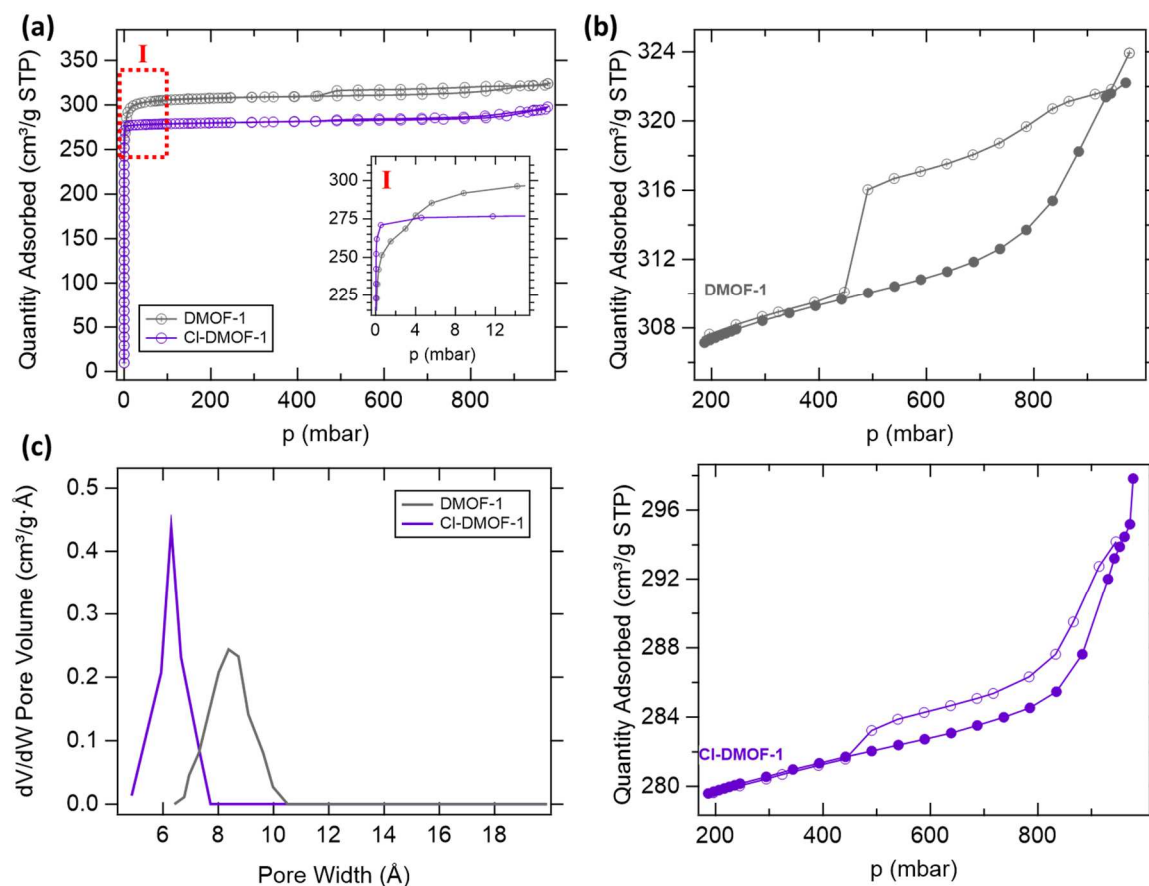
### 8.1. N<sub>2</sub>-Sorption characteristics of bulk Cl-DMOF-1 and DMOF-1

Applying a certain pressure of a selected adsorbate on flexible MOFs switches their structure between an open and closed phase.<sup>[9,10]</sup> The pressure at which the switching of the structure occurs is termed as gate-opening and gate-closing pressure and depends both on the adsorbate and on the flexibility of the framework. Since different sorbates (*i.e.*, N<sub>2</sub>, CO<sub>2</sub>, C<sub>2</sub>H<sub>4</sub>) will interact with the MOF pores in a characteristic and distinct manner, not every adsorbate will trigger the gate-opening process, as it was shown by Zhu et. al in the case of the 4,4'-azopyridine linkers of the pcu-5-Zn MOF when employing N<sub>2</sub> as the adsorbate.<sup>[9]</sup> It has been further demonstrated that ligand flexibility can modulate the gate-opening pressures.<sup>[9,11]</sup> Moreover, the dimension of the MOF crystallite has a discernible impact on the switchability and gate-opening behavior.<sup>[12]</sup> Smaller crystallite sizes, as observed in N<sub>2</sub> adsorption experiments with ZIF-8, are associated with an increase of the gate-opening pressure and hysteresis width.<sup>[13a]</sup> Typically, a certain critical crystallite size is required above which the adsorbate uptake hysteresis can be observed, where the specific size depends on the chemical composition of the MOF<sup>[12]</sup> Exemplarily, in pillared MOFs containing *dabco*, the critical crystallite size is typically in the range of several hundred of nanometers (*i.e.*, Cu<sub>2</sub>(DE-bdc)<sub>2</sub>(*dabco*) = 430 nm; DUT-8 = 500 nm).<sup>[12]</sup> Hence, downsizing of MOF crystallites might suppress the gating (closed-to-open) and breathing (open-narrow-open) MOF pore transitions, or lead to a shift of the gate-opening and -closing pressures.<sup>[12]</sup>

To ascertain, whether the chlorine functionalization of the DMOF-1 system yielding the Cl-DMOF-1 will alter the flexibility of the structure, we have performed sorption measurements using N<sub>2</sub> as the adsorbate. The calculated BET surface area for DMOF-1 is 1290.6 ± 3.5 m<sup>2</sup>/g, whereas Cl-DMOF-1 exhibits a lower surface area of 1196.3 ± 0.5 m<sup>2</sup>/g. In Figure S13a, the respective isotherms are shown, with the non-functionalized DMOF-1 system comprising a higher physisorption compared to Cl-DMOF-1. Moreover, the nitrogen adsorption capacity of DMOF-1 was determined with 324 cm<sup>3</sup>/g, while Cl-DMOF-1 shows an N<sub>2</sub> adsorption capacity of 298 cm<sup>3</sup>/g. Both structures exhibit N<sub>2</sub> isotherm of type I,<sup>[13b]</sup> where a subtle step is observed for DMOF-1 in the adsorption branch (~2.5 mbar) as shown in the inset in Figure S13a. This

behavior is not observed in the Cl-DMOF-1 samples, which might be attributed to the formation of a more rigid system. Both materials exhibit small hysteresis in N<sub>2</sub> isotherms above 400 mbar (closing point at  $PIP_0 = 0.45$ ), which is attributed to capillary condensation within mesoscale features as already reported by Wang et al.<sup>[14a]</sup>. This behavior has already been observed for DMOF-1 type systems and has been attributed to the presence of crystal defects.<sup>[14b]</sup>

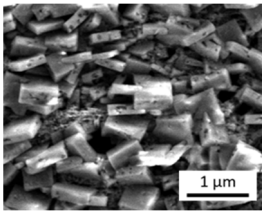
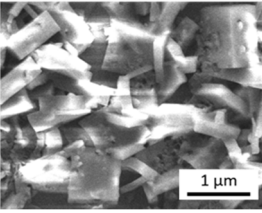
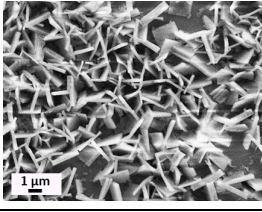
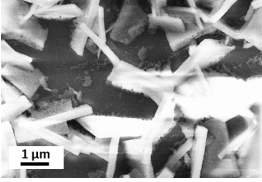
The pore size distribution of both materials was determined using the Non-Local Density Functional Theory NLDFT method. The pore size distribution is centered at 8 Å for DMOF-1 and 6 Å for Cl-DMOF-1 (Figure S13c), where the prior is in good agreement with literature.<sup>[7a]</sup> These values are comparable to other findings reported on DMOF-1 isoreticular analogues.<sup>[7c]</sup> Hence, the results can be ascribed to the additional functional groups localized in the framework voids, which increase molecular weight and density and decrease the accessible free volume compared to unmodified parent structures. This is corroborated by the considerably lower N<sub>2</sub> quantity adsorbed by Cl-DMOF-1 (Figure S13a), which is also reflected by the distinctly fewer azobenzene molecules per pore determined both for bulk Cl-DMOF-1 and the film structure Cl-DMOF-1<sub>90min</sub> (see SI chapter 6). The comparably lower surface area and median pore size of Cl-DMOF-1 with respect to its parent DMOF-1 could be explained by the space occupation of Cl substituents in the terephthalate linker.<sup>[15]</sup> It must be noted, that the crystallite sizes for these two structures was determined by SEM measurements to be ~3 μm.



**Figure S13** N<sub>2</sub> sorption isotherms of **(a)** CI-DMOF-1 (purple) and DMOF-1 (grey). The marked area (I) is shown as a zoom-in on the region displaying a weak opening of the DMOF-1 pores upon N<sub>2</sub> adsorption. This behaviour is absent for CI-DMOF-1. **(b)** The adsorption and desorption branches are displayed as solid and open markers, respectively. **(c)** The calculated pore size distribution (DFT) for the respective structures is displayed with 8 Å DMOF-1 and 6 Å for CI-DMOF-1.

## 9. Comparison of chemical and physical properties between CI-DMOF-1 and DMOF-1 (film, bulk)

**Table S3** Comparison of the DMOF-1 film structure reported in ref. 2 and the herein investigated CI-DMOF-1 film structure.

Film structure	Crystal size distribution	Average film thickness ( $\mu\text{m}$ )	Azobenzene loading (at average thickness)	Time of structural response (sec) <sup>c</sup>	SEM image	Opening of micropores of bulk system (mbar)
DMOF-1 <sup>a</sup>	n.d. <sup>b</sup>	~0.4	---	---		2.5
DMOF-1/AB <sup>a</sup>	45%		1 molecule/pore	15		---
CI-DMOF-1	49%	~1.3	---	---		no
CI-DMOF-1/AB	32%		<0.5 molecule/pore	60		---

<sup>a</sup> values and related information taken from ref. 2.

<sup>b</sup> not determined in ref. 2.

<sup>c</sup> evaluated from time-resolved GIWAXS measurements considering the (001) reflection.

## References

- [1] Linares-Moreau, M., Brandner, L. A., Kamencek, T., Klokic, S., Carraro, F., Okada, K., Takahashi, M., Zojer, E., Doonan, C. J., Falcaro, P., *Adv. Mat. Interfaces* **2021**, *8*, 2101039.
- [2] Klokic, S., Naumenko, D., Marmioli, B., Carraro, F., Linares-Moreau, M., D. Zilio, S., Birarda, G., Kargl, R., Falcaro P., and Amenitsch, H.; *Chem. Sci.*, **2022**, *13*, 11869–11877.
- [3] Amenitsch, H., Rappolt, M., Kriechbaum, M., Mio, H., Laggner, P., Bernstorff, S., *J. Synchrotron Rad.* **1998**, *5*, 506.
- [4] Burian, M., Meisenbichler, C., Naumenko, D. & Amenitsch, H.; *J. Appl. Crystallogr.* **2022**, *55*, 677–685.
- [5] a) Lupi, S., Nucara, A., Perucchi, A., Calvani, P., Ortolani, M., Quaroni, L., Kiskinova, M., *J. Opt. Soc. Am. B* **2007**, *24*, 959. b) Birarda, G., Bedolla, D., Piccirilli, F., Stani, C., Vondracek, H., Vaccari, L., *Proc. SPIE 11957, Biomedical Vibrational Spectroscopy 2022: Advances in Research and Industry*, 1195707, **2022**. c) Webb, J. D., Neidlinger, H. H., Connolly, J. S., *Polymer Photochemistry* **1986**, *7*, 503-513.
- [6] Ambroz, F.; Macdonald, T. J.; Martis, V.; Parkin, I. P. *Small Methods* **2018**, *2*.
- [7] a) Yanai, N., Uemura, T., Inoue, M., Matsuda, R., Fukushima, T., Tsujimoto, M., Isoda S., and Kitagawa, S; *J. Am. Chem. Soc.*, **2012**, *134*, 4501–4504. b) Griffiths, K., Halcovitch N. R., and Griffin, J. M., *Chem. Mater.*, **2020**, *32*, 9925–9936. c) Xie, M.; Prasetya, N.; Ladewig, B. P. *Inorg. Chem. Commun.*, **2019**, *108*, 107512.
- [8] Koehler, T., Strauss, I., Mundstock, A., Caro, J., Marlow, F., *J. Phys. Chem. Lett.*, **2021**, *12*, 8903-8908.
- [9] Zhu, A.; Yang, Q.; Mukherjee, S.; Kumar, A.; Deng, C.; Bezrukov, A. A.; Shivanna, M.; Zaworotko, M. J. *Angew. Chem., Int. Ed.*, **2019**, *58*, 18212–18217.
- [10] Krause, S.; Bon, V.; Senkovska, I.; Többens, D. M.; Wallacher, D.; Pillai, R. S.; Maurin, G.; Kaskel, S.; *Nat. Commun.*, **2018**, *9*.
- [11] Mercedes K. Taylor, Tomče Runčevski, Julia Oktawiec, Miguel I. Gonzalez, Rebecca L. Siegelman, Jarad A. Mason, Jinxing Ye, Craig M. Brown, and Jeffrey R. Long, *J. Am. Chem. Soc.*, **2016** *138* (45), 15019-15026
- [12] Ehrling, S., Miura, H., Senkovska I., and Kaskel, S.; *Trends Chem.*, **2021**, *3*, 291–304.
- [13] a) Watanabe, S., Ohsaki, S., Hanafusa, T., Takada, K., Tanaka, H., Mae K., and Miyahara, M. T.; *Chemical Engineering Journal*, **2017**, *313*, 724–733. b) Thommes, M. K., Neimark, V., J. P. Olivier, J. P., Rodriguez-Reinoso, F., Rouquerol J. and Sing, K. S. W., *Pure Appl. Chem.*, **2015**, *87*, 1051–1069.
- [14] a) Wang, Z. and Cohen, S. M., *J. Am. Chem. Soc.*, **2009**, *131*, 16675–16677. b) Gregg, S. J.; Sing, K. S. W. *Adsorption, Surface Area, and Porosity*, 2<sup>nd</sup> ed.; Academic Press: London, **1982**.
- [15] Senkovska, I.; Bon, V.; Abylgazina, L.; Mendt, M.; Berger, J.; Kieslich, G.; Petkov, P.; Luiz Fiorio, J.; Joswig, J.; Heine, T.; et al. *Angew. Chem., Int. Ed.*, **2023**, *62*.